








RESEARCH ARTICLE | JANUARY 25 2023

A turbulent crosswind simulation method at high-speed railway tunnel entrance: Based on field test and geometric turbulence generator

E Deng (邓鐸) ; Huan Yue (岳欢) ; Yi-Qing Ni (倪一清) ; You-Wu Wang (王友武)  ;
Xu-Hui He (何旭辉) ; Zheng-Wei Chen (陈争卫) 



Physics of Fluids 35, 015156 (2023)

<https://doi.org/10.1063/5.0133292>



Articles You May Be Interested In

How do crosswinds from two turbulent generators affect the aerodynamic loads of running trains at tunnel entrances?

Physics of Fluids (December 2023)

Wake dynamic characteristics of windproof structures in embankment–bridge sections along a high-speed railway under natural strong crosswinds

Physics of Fluids (May 2023)

Acceleration and Reynolds effects of crosswind flow fields in gorge terrains

Physics of Fluids (August 2023)



Physics of Fluids

Special Topics Open
for Submissions

[Learn More](#)

A turbulent crosswind simulation method at high-speed railway tunnel entrance: Based on field test and geometric turbulence generator

Cite as: Phys. Fluids **35**, 015156 (2023); doi: [10.1063/5.0133292](https://doi.org/10.1063/5.0133292)

Submitted: 2 November 2022 · Accepted: 4 January 2023 ·

Published Online: 25 January 2023



View Online



Export Citation



CrossMark

E Deng (邓鐸),^{1,2}  Huan Yue (岳欢),³  Yi-Qing Ni (倪一清),^{1,2}  You-Wu Wang (王友武),^{1,2,a)} 
Xu-Hui He (何旭辉),^{3,4}  and Zheng-Wei Chen (陈争卫)^{1,2} 

AFFILIATIONS

¹National Rail Transit Electrification and Automation Engineering Technology Research Center (Hong Kong Branch), Hong Kong, People's Republic of China

²Department of Civil and Environmental Engineering, The Hong Kong Polytechnic University, Hong Kong, People's Republic of China

³School of Civil Engineering, Central South University, Changsha, People's Republic of China

⁴National Engineering Research Center of High-speed Railway Construction Technology, Changsha, People's Republic of China

^{a)} Author to whom correspondence should be addressed: youwu.wang@polyu.edu.hk

ABSTRACT

It is common for high-speed trains (HSTs) to abruptly switch between a tunnel and a flat ground along high-speed rail lines. When encountering strong crosswinds, the safety of HSTs in such running scenarios will be severely threatened. The simulation of the turbulent component of an incoming crosswind is very important to restore the real aerodynamic environment of HSTs in tunnel-flat ground-tunnel (TFT) running scenario. The purpose of the present study is to determine which of the two geometric turbulence generators, the spire and the fence, is more suitable for computational fluid dynamics (CFD) simulation of a fluctuating crosswind field in the TFT scene. First, the wind field characteristics in the TFT scene are analyzed based on the field test. Then, the tunnel-flat ground-spire/fence CFD model was established based on the “mosaic” mesh technology. Finally, the difference of wind field fluctuating characteristics under two turbulence generator conditions based on improved delayed detached eddy simulation (IDDES) is discussed. The main results show that the average wind speed of the windward and leeward lines in the fence case are 60% and 43.75% higher than the corresponding values in the spire case, respectively. The main conclusions show that the turbulent crosswind generated by the spire is more consistent with the spectrum characteristics of the natural wind field.

Published under an exclusive license by AIP Publishing. <https://doi.org/10.1063/5.0133292>

I. INTRODUCTION

It is common for high-speed trains (HSTs) to abruptly switch between tunnel and flat ground along high-speed rail lines. When encountering strong crosswinds, the safety of HSTs in such running scenarios will be severely threatened. The tunnel-flat ground-tunnel (TFT) scene has complex topographic characteristics, which determines that the natural strong crosswind flow in this area often has complex turbulent components rather than simple constant wind. In fact, the simulation of the turbulent component of the incoming crosswind is very important to restore the real aerodynamic environment of HSTs in TFT running scenario.¹ Currently, the methods used to simulate turbulent incoming flow mainly include empirical formula,² wind tunnel simulation,³ and Computational Fluid Dynamics (CFD) numerical simulation.⁴ Spires⁵ and fences⁶ are often used as incoming

turbulence generators for wind tunnel tests and numerical simulations. Due to the difference in the shape of the two structures, there are significant differences in the performance of the turbulent flow field generated at the tunnel entrance. Considering the importance of ensuring the running safety of HST, it is not clear which spire or fence is more suitable for simulating the fluctuating incoming flow field at the high-speed railway tunnel entrance.

Some researchers have carried out a series of research on the performance of turbulence field generated by physical turbulence generators in the wind tunnel laboratory. In order to study the influence of incoming wind on the wind-induced acceleration and aerodynamic damping ratio of square high-rise buildings, Li *et al.*⁷ and Tominaga and Shirzadi⁸ used the spire and rough element model to simulate the atmospheric boundary layer (ABL) in the wind tunnel laboratory.

To study the influence of turbulence integral scale, Du *et al.*⁶ conducted wind tunnel tests on four rectangular models under turbulent flow conditions generated by fences and obtained the characteristics of fluctuating pressure on the windward side under corresponding conditions. Górski *et al.*⁹ studied the effects of wind turbulence on the average aerodynamic drag, lift, and moment coefficients of the stationary ice-accreted section model of a bridge cable for different turbulent flow conditions generated by fences. Dawi and Akkermans¹⁰ studied the aeroacoustics of general vehicles in a turbulence wind tunnel and verified it with detached eddy simulation. Kozmar and Laschka³ realized three urban ABL simulations in the wind tunnel by using three physical turbulence generators, namely, Counihan vortex generator, castellated barrier wall, and surface roughness elements. The results show that the simulation length scale in wind tunnel research focusing on structural wind load may be larger when ABL simulation is carried out with a truncated Counihan vortex generator.

The physical wind tunnel tests are often costly. The generation of inflow turbulence often requires that the generated inflow is divergence-free and meets the basic target statistical characteristics, including the two-point statistical characteristics and spatial correlation of the flow described by the coherence function. Shen *et al.*⁵ adopted the weighted wave superposition method to generate fluctuating wind field as the inlet condition for the study of urban wind environment. By comparing the wind field performance generated by spires and roughness elements, the feasibility of this method was ensured. Melaku and Bitsuamlak¹¹ proposed a comprehensive inflow turbulence generation technology with well-defined two-point flow statistics based on the spectral representation method. Compared with the wind field measurement results of boundary layer wind tunnel laboratory, the effectiveness of the proposed method in representing one-point statistics and two-point statistics is verified. Xue *et al.*⁴ proposed a synthetic turbulence generator based on a lattice Boltzmann method (LBM) at the interface of the Reynolds averaged Navier–Stokes (RANS) equations and the LBM large eddy simulation (LES). Hu *et al.*¹² proposed a spectral element method for LES turbulence generation at the inlet, which can accurately predict the average wind speed and turbulence intensity distribution in hilly terrain, and overcoming the difficulty of completely meeting the specified turbulent characteristics, spectrum, and time-correlation. However, the results generated by the above methods are often verified by comparing with the results of the scaled wind tunnel test, and the turbulence integration scale is difficult to reach the level of the actual wind field.

The influence of turbulent wind flow with complex fluctuating components on the aerodynamic effects of HST may be more prominent in complex scenarios, such as TFT. Some researchers have studied the aerodynamic performance of HST under turbulent wind conditions, and few researchers have focused on the sudden change in turbulent wind at the high-speed railway tunnel entrance. Cheli *et al.*¹³ generated turbulent incoming flow through the spires in the wind tunnel and studied the aerodynamic forces on the train body under the action of incoming crosswind at different turbulence integral scales. The results show that under the action of turbulent incoming flow with higher integral length scale, the lateral force, lift force, and overturning moment of the train increase. In order to study the aerodynamic characteristics of HSTs in the ABL, Niu *et al.*¹⁴ conducted different ABL simulations by changing the inflow conditions of different turbulence intensities generated by the spire spacing in the wind

tunnel. Noguchi *et al.*¹⁵ studied the influence of yaw angle and distance from upstream boundary to embankment on the aerodynamic force of the train under turbulent wind generated by the spire through LES numerical simulation and wind tunnel experiment. The study also purposely compares the difference between the influence of smooth and ABL incoming flows on the vortex structures around the train body. Zhu *et al.*¹⁶ studied the aerodynamic admittance of rail vehicles on three typical railway infrastructure forms under turbulent inflow conditions generated by fences in the wind tunnel. However, no researchers have systematically compared the difference between the spire and fence on the performance of turbulent crosswind field simulation based on the field test results of TFT.

In order to determine which of the two geometric turbulence generators, the spire and the fence, is more suitable for CFD simulation of fluctuating crosswind field in TFT scene, the present study intends to conduct systematic comparative analysis of wind field characteristics under the conditions of two geometric turbulence generators based on on-site wind field test and improved delayed detached eddy simulation (IDDES) method. The rest of the paper is organized as follows. The analysis of wind field characteristics in the TFT scene based on the field test is introduced in Sec. II. CFD numerical method and validation are described in Sec. III. The difference of wind field fluctuating characteristics under two turbulence generator conditions based on IDDES are presented in Sec. IV. The conclusions are arranged in Sec. V. The main contribution of this paper is to propose a turbulent crosswind simulation method for the study of aerodynamic performance of moving HSTs at the tunnel entrance.

II. FIELD TEST OF WIND FIELD

A. Measuring point arrangement

The field test is carried out in a typical TFT site along the Wuhan–Guangzhou high-speed railway in China.¹⁷ The fluctuating wind speed is measured by a Gill Wind Master Pro 3D ultrasonic anemometer. The sampling frequency is 32 Hz. The test will be carried out from March to September 2021. During this period, the sensors did not work without interruption. In most of the periods of low wind speed, the sensors stopped working and only started sampling during the periods of high wind speed. The tunnel is a standard double-line section of 100 m², and the portal type is a hat oblique type. The length of the open section is approximately 2.79 L (L , the full length of a three-carriages train, 76.65 m). The layout of the measuring points is shown in Fig. 1, and the two measuring points are arranged on the west side of the line. Taking tunnel 1 as the starting point, the numbers are 1# and 2#, and the distances between the corresponding measuring points and the entrance of the tunnel 1 are 0.26 and 0.52 L , respectively.

B. Average wind speed and direction

The process of an eight-carriage HST leaving the tunnel often does not exceed 3 s. Therefore, a 3 s time interval is used for segmentation for the time-history data collected in a period of six consecutive hours when the strongest wind. Figure 2 shows the average wind speed and direction for each sample as a rose diagram. In the figure, the samples with wind speed lower than 3.4 m/s have been eliminated.¹⁸ The calculation equations for the average wind speed and direction of each sample are as follows:

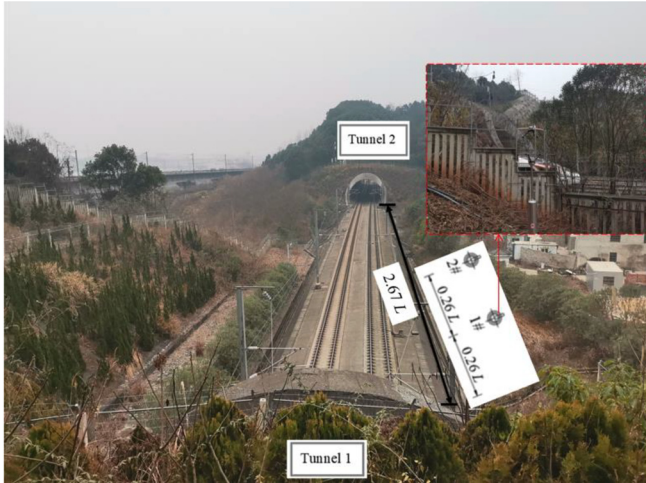


FIG. 1. Schematic of the measuring point layout of the TFT section.

$$\bar{U} = \frac{1}{n} \sum_{i=1}^n \sqrt{U_{Hi}^2 + U_{wi}^2}, \quad (1)$$

$$\bar{\theta} = \frac{1}{n} \sum_{i=1}^n \theta_i, \quad (2)$$

where \bar{U} and $\bar{\theta}$ denote the average wind speed and the average wind direction angle of each 3 s sample, respectively, and n is the number of samples.

The following findings are obtained from Fig. 2: The high wind speed section of 1# and 2# measuring points is mainly 9–14 m/s. The maximum average wind speeds of 1# and 2# measuring points are 13.9 and 14.1 m/s, respectively, and the average wind direction of the mainstream is almost perpendicular to the line direction.

C. Turbulence intensity

Turbulence intensity has an important influence on the buffeting effect of HSTs under crosswind. The mainstream wind direction is

perpendicular to the train running line, and the u component is defined as the direction of vertical blowing to the line. The turbulence intensity (I_u) on the u component of each sample is calculated by the following equations:

$$\sigma_u = \sqrt{\frac{\sum_{i=1}^n (U_{ui} - \bar{U}_u)^2}{n-1}}, \quad (3)$$

$$I_u = \frac{\sigma_u}{\bar{U}}, \quad (4)$$

where u is component of the wind speed at a certain time of U_{ui} , and σ_u represents the standard deviation of u component wind speed in 3 s sample.

The probability density function (PDF) distribution of natural wind turbulence often conforms to the lognormal distribution and is expressed as follows:

$$f(x) = \frac{1}{x\sigma\sqrt{2\pi}} e^{-\frac{(\ln x - \mu)^2}{2\sigma^2}}; \quad x > 0, \quad (5)$$

where the fitting parameters μ and σ represent the expected value and standard deviation of the natural logarithm of the variable, respectively, thereby determining the position of the peak point of the fitting curve and the degree of dispersion of the data.

Figure 3 shows the scatterplot of the turbulence intensity in the u direction of the samples at measuring points 1# and 2# as a function of average wind speed to understand the variation of turbulence intensity further with average wind speed in the TFT site scenario. Figure 4 shows the turbulence intensity PDF fitting curve comparison chart of 1# and 2#, and Table I shows the turbulence degree PDF fitting parameters.

The following findings are obtained from Fig. 3: The number of turbulence intensity samples in the u direction is large and the distribution range is wide (in the range of 0–1) when the average wind speed is low. With the increase in average wind speed and when wind speed exceeds 10 m/s, the turbulence intensity of the 1# measuring point is between 0.1 and 0.3, and that of the 2# measuring point

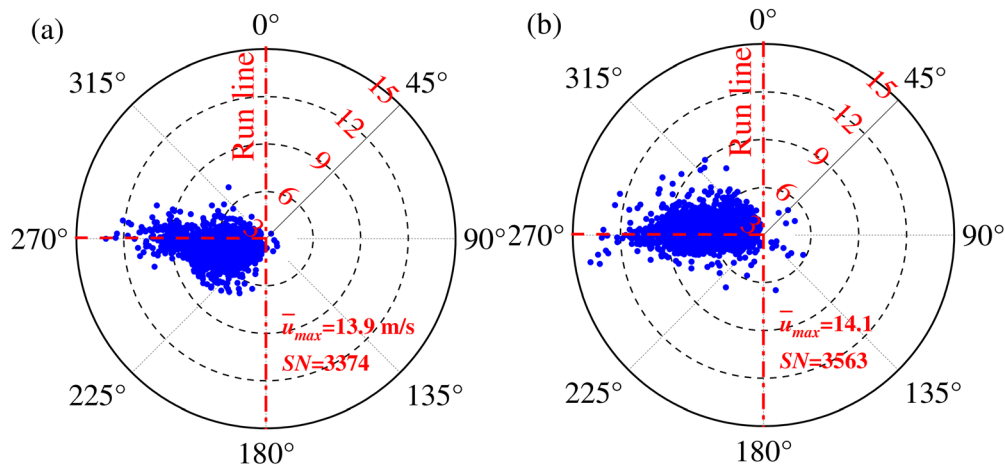


FIG. 2. Rose diagram of the wind speed and direction: (a) 1# and (b) 2#.

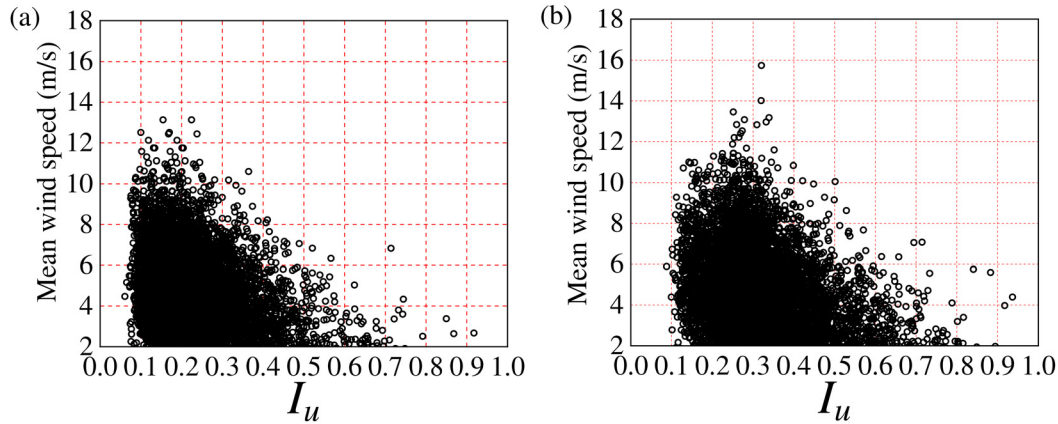


FIG. 3. Turbulence degree-mean wind speed scatterplot: (a) 1# and (b) 2#.

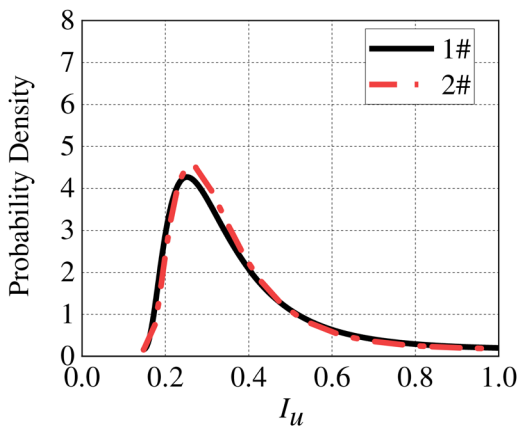


FIG. 4. Comparison of turbulence intensity PDF fitting curves.

TABLE I. Fitting parameters of turbulence intensity PDF.

| Measuring points | I_u | | |
|------------------|--------|----------|-------|
| | μ | σ | R^2 |
| 1# | -1.031 | 0.235 | 0.962 |
| 2# | -1.016 | 0.219 | 0.968 |

decreases rapidly to 0.3. Figure 4 and Table I show no substantial difference between the σ and μ of 1# and 2# measuring points, and the turbulence intensity trend of the two measuring points is consistent with the expected value of PDF. Therefore, 0.3 can be selected as the representative value of the turbulence intensity of the tunnel entrance.

D. Spectrum analysis

Yang *et al.*¹⁷ pointed out that in the u direction, the von Karman spectrum is suitable for describing the power spectrum expression of the fluctuating wind field at the tunnel entrance, and the frequency

domain coherence function is provided to study the statistical coherence of turbulence between two points. Its equation is as follows:

$$\frac{f \cdot S_u(f, z)}{\sigma_u^2} = \frac{a \cdot \frac{L_u \cdot f}{\bar{U}} \left[1 + b \cdot \left(\frac{L_u \cdot f}{\bar{U}} \right)^2 \right]}{\left[1 + c \cdot \left(\frac{L_u \cdot f}{\bar{U}} \right)^2 \right]^{\frac{d}{6}}}, \quad (6)$$

where a , b , c , and d are the fitting parameters; L_u denotes the length scale of turbulence integral in u direction, and its calculation equation is as follows:

$$L_u = 0.146 \cdot \frac{\bar{U}}{f_p}, \quad (7)$$

where f_p is the frequency corresponding to the peak of the fitted von Karman spectrum,

$$\text{Coh}(f) = K \cdot \exp \left(-C \cdot \frac{f \cdot \Delta}{\bar{U}} \right), \quad (8)$$

where C represents the attenuation coefficient, Δ represents the distance between two points, z represents the distance between the measuring point and the ground, \bar{U} represents the average wind speed of the sample, and B and K are the fitting parameters.

Figure 5 shows the measured average power spectrum of the two measuring points after dimensionless processing and its corresponding fitting curve. Table II shows the von Karman spectral fitting parameters of the measuring points. Figure 6 shows the measured results of the coherence function between the measuring points (the length of the Hanning window is 4096) and the corresponding fitting curve.

When frequency is close to 0, the measured coherence function value is not equal to 1, indicating that Eq. (8) can achieve the ideal fitting effect. K decreases with the increase in the distance between the two points, whereas C increases with the increase in the distance. This phenomenon can be explained as follows: When the distance between the two measuring points is equivalent to the turbulence integral scale, the coherence of the spectrum is inversely proportional to the distance

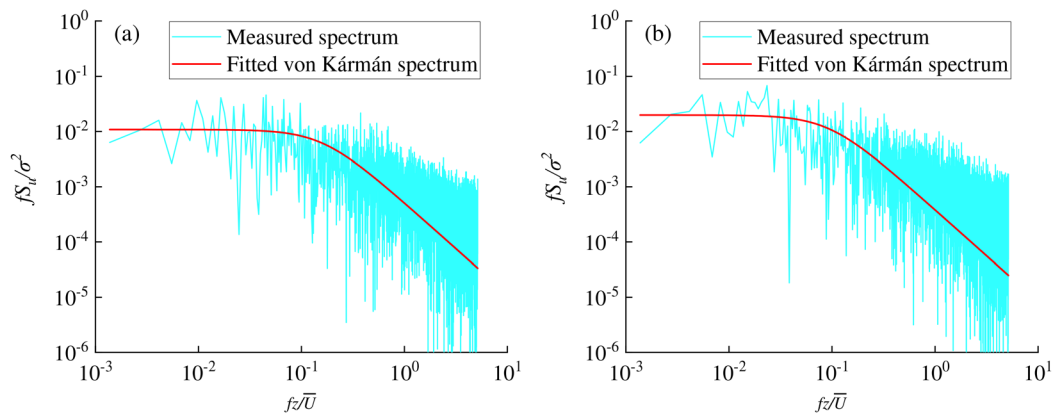


FIG. 5. Wind power spectrum and corresponding fitted curve: (a) 1# and (b) 2#.

TABLE II. Von Karman spectral fitting parameters of measuring points.

| Measuring points | u | | | |
|------------------|------|-----|------|----|
| | a | b | c | d |
| 1# | 25.3 | 3.6 | 22.2 | 11 |
| 2# | 25.2 | 3.6 | 22.3 | 11 |

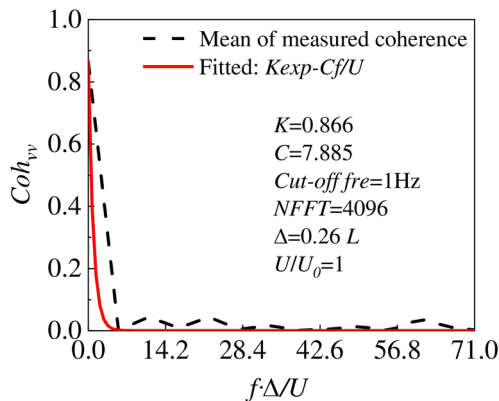


FIG. 6. Coherence function and fitting results between 1# and 2#.

in general. K reflects the coherence of the spectrum of the two measuring points when the frequency approaches 0 and the attenuation coefficient C determines the coherence of the high frequency part.

The following findings are obtained from Figs. 5 and 6:

The von Karman spectrum can better fit the power spectrum of the two measuring points, and the von Karman spectrum fitting parameters of the two measuring points are close. In the low frequency band where the frequency domain tends to 0, the ordinate value is approximately 0.86, and the points on both sides have strong coherence. The spectral coherence effective distance of turbulence on u component at each measuring point in the tunnel entrance section can be estimated by setting the coherence threshold to 0.7. The turbulence

integral scales of 1# and 2# measuring points are 50.4 and 58.6 m, respectively.

III. CFD METHOD

A. Geometry and boundary conditions

Figure 7 shows the overall layout of the tunnel-flat ground-spire/fence geometric computational domain and the setting of each boundary condition. The width (W) and height (H) of the CRH380B train carriage are 3.625 and 3.89 m, respectively. The tunnel model is modeled with reference to the inner contour of the 350 km/h double-track tunnel. The clearance area is 100 m^2 and the length is $2L$. The track slab is established in according to the specification requirements, and its specific size is shown in Fig. 7. In the open line section on the flat ground, the slope height of the tunnel entrance is $5.34 H$, the full height of the atmospheric area is $15.37 H$, the top length is $2.44 L$, and the full width is $33.10 W$. The spire/fence is $2.76 W$ from the windward side line (WSL). The size and the layout of the spire are shown in Fig. 8(a). The spire in the Wind Tunnel Laboratory of the National Engineering Laboratory for High-speed Railway Construction of Central South University is magnified eight times. The height of the spire is $5.08 H$, and the width of the bottom is $0.05 L$. The bottom spacing is $0.05 L$; 19 spacings are available, and the blockage rate of the bright line segment is 7.1%.¹⁴ The size and the layout of the fence are shown in Fig. 8(b). The blocking rate of the open line section is consistent with the spire model. The total length of the fence is $1.98 L$, the height is $5.33 H$, the square hole width is $0.05 L$, and the rib width is $0.014 L$. The running line of the HST near the spire is the WSL, and a measuring point is arranged at an interval of $0.13 L$. The farther running line is called the leeward side line (LWS). The three measuring points (P1, P2, and P3) are located at the edge of the windward line, namely, 0, 0.26, and $0.52 L$ away from the tunnel entrance, respectively, and their heights is $0.64 H$. The measuring lines in the three directions of x , y , and z are arranged with three measuring points as the center.

Figure 7 also shows the boundary conditions of the model. The velocity inlet boundary condition is applied to the incoming flow surface of the open-line atmospheric domain. The symmetry boundary condition is applied to the top surface of the atmospheric domain at the tunnel exit. The no-slip wall boundary condition is used for the

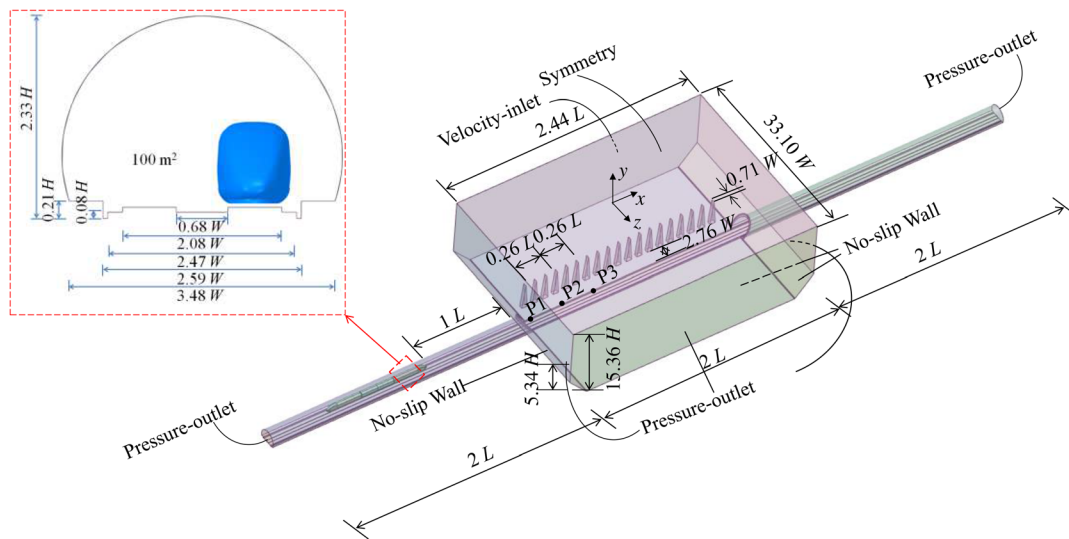


FIG. 7. Calculation domain and boundary conditions of the full-scale model.

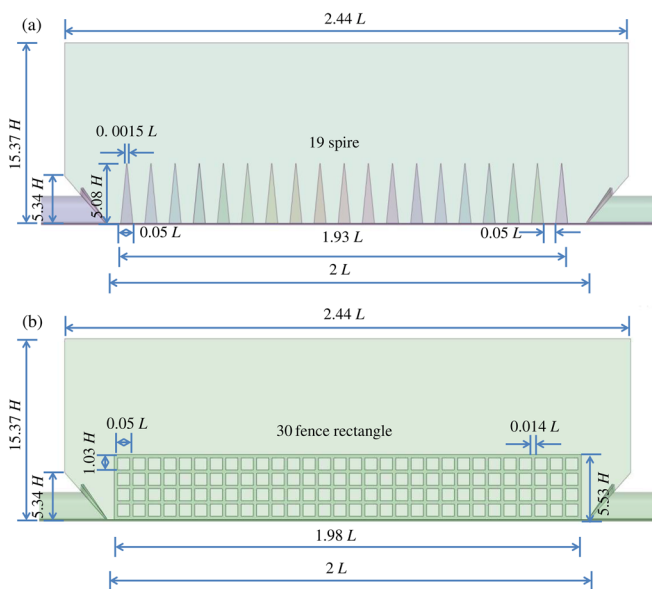


FIG. 8. Calculation domain and size of the numerical model: (a) spire and (b) fence.

solid walls such as the spire surface, ground surface, tunnel wall, and the walls on both sides of the tunnel entrance. The pressure-outlet boundary condition is used for the remaining atmospheric outlet interface.

B. Meshing strategy

Based on the “mosaic” mesh technology of Fluent Meshing 2020R2, the computational domain of the CFD model is meshed. Compared with the traditional structured and unstructured meshes,

mosaic mesh technology combined with the IDDES model can solve the full-scale model and ensure efficiency and accuracy. The total number of grid cells in all models is approximately 45×10^6 . Figure 9 shows the grid model by taking the fence model as an example. The Poly-Hexcore body grid is used for discretization in the static grid area (B). The grid size range of the spire/fence surface is 0.05–0.1 m. Five boundary layers are setup. The grid size of the spire/fence is gradually enlarged from the inside to the outside by setting the refined area. The size of the refined area is limited to 0.2 m, and the grid size on the outermost boundary is approximately 1 m. In the present study, the train model in the dynamic grid area (A) is set to be stationary. The grid details of the dynamic grid area are described in detail in Ref. 19.

C. Solution strategy

The accurate turbulence models based on numerical simulation mainly include LES and IDDES. The basic idea of the LES method is to filter the Navier–Stokes equation to solve the large-scale vortex structure directly, and the turbulence smaller than the filter scale is described by the existing model. It can capture more accurate transient flow field information compared with RANS. The IDDES model combines the advantages of the RANS and LES methods.²⁰ The RANS model is used to solve the grids with turbulence scale smaller than the maximum grid size near the solid wall boundary. The large scale unsteady turbulence dominated region is solved directly by LES. The IDDES model simultaneously solves the transition problem of RANS and LES. The IDDES grid resolution requirement is greatly reduced compared with LES, thereby reducing calculation cost and ensuring calculation accuracy.

In this study, the IDDES model is used to solve the air-tunnel-flat ground-spire/fence CFD model. Based on the Fluent 2020R2, the finite volume method and the pressure-based solver are used to solve the transient solution of the incoming wind field. The method of least squares is also used to calculate the gradient of the control body

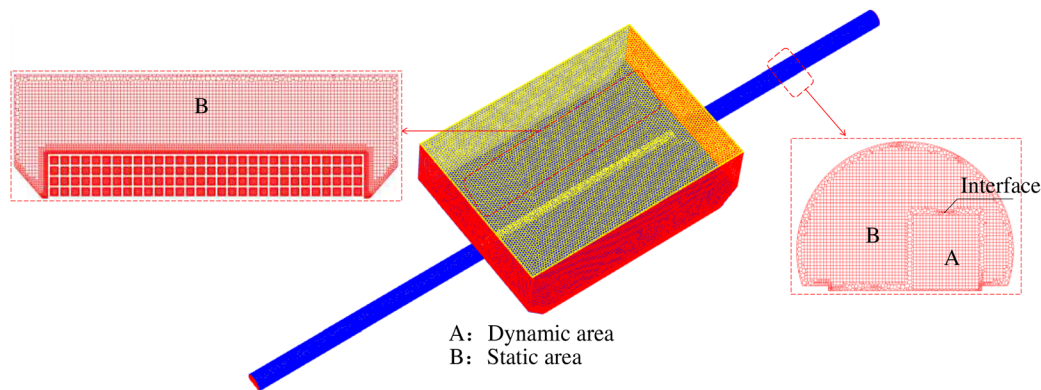


FIG. 9. Display of the meshing model.

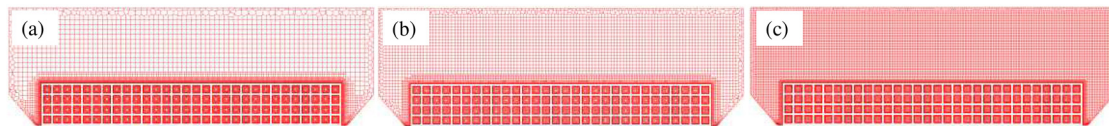


FIG. 10. Three grid models with different grid resolutions (a) fence C, (b) fence M, and (c) fence F.

around the grid element. The semi-implicit algorithm of pressure–velocity coupling equation is used to deal with the pressure–velocity coupling equation. The bounded central difference scheme and the second-order upwind scheme are used to solve momentum equation and time integration, respectively. The time discretization adopts the unsteady calculation method of double time step format. The physical time step is set to 10^{-4} s, the number of iteration steps of each time step is preset to 50 steps, and the residual is set to 10^{-6} . All models are calculated in the Wuxi Supercomputing Center, China. Each model is calculated with 144 cores, and the calculation requires approximately 10 days.

D. Analysis of meshing independence

The fence model is considered an example to analyze the sensitivity of the calculation results of the model to the influence of grid size. The grid models of low, medium, and high resolutions are established by adjusting the grid size parameters of the barrier model (Fig. 10). The total grid number of the three models is 35×10^6 (fence C), 45×10^6 (fence M), and 55×10^6 (fence F). Incoming wind with a constant speed of 20 m/s is applied in the Z (u) direction to monitor the wind speed time history of the P3 measuring point on the train running line. Figure 11 compares the monitoring indices of grid models with different resolutions.

The calculation results of the model with 45×10^6 grid elements agree with those of the model with 55×10^6 grid elements. The calculation results of the low-resolution model deviate from those of the high-resolution grid and are not synchronized with the high and medium-resolution grids. Therefore, using a model with 45×10^6 grid elements is reasonable.

IV. DIFFERENCE OF WIND FIELD CHARACTERISTICS

A. Spatial distribution of wind speed

The wind speed of 20 m/s is applied at the model velocity inlet to calculate 180 s to reveal the spatial distribution difference of the flow

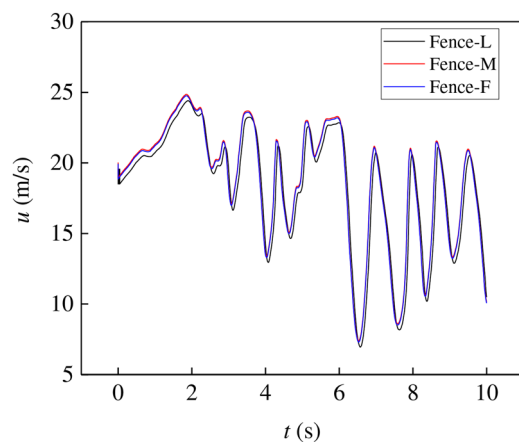


FIG. 11. Comparison of the wind velocity time history of 3# under different grid resolution conditions.

field at the tunnel entrance simulated by the spire and the fence. Figures 12 and 13 show the turbulent wind time history along the measuring line calculated by the numerical model of the two turbulence generators of the spire and the fence. The following findings are obtained from Fig. 14.

For the spire, the wind speed near the spire increases in the direction of incoming flow, due to the acceleration effect of the spire. The P2 and P3 lines are consistent, with an average wind speed of 1.4. Except for P1, the other lines decay to a steady state at 2.76 W. The wind speed of P1 is smaller than that of P2 and P3 due to the distance between the spire and the mountain wall. However, with the attenuation of the incoming turbulence, the average wind speed of the P2 and

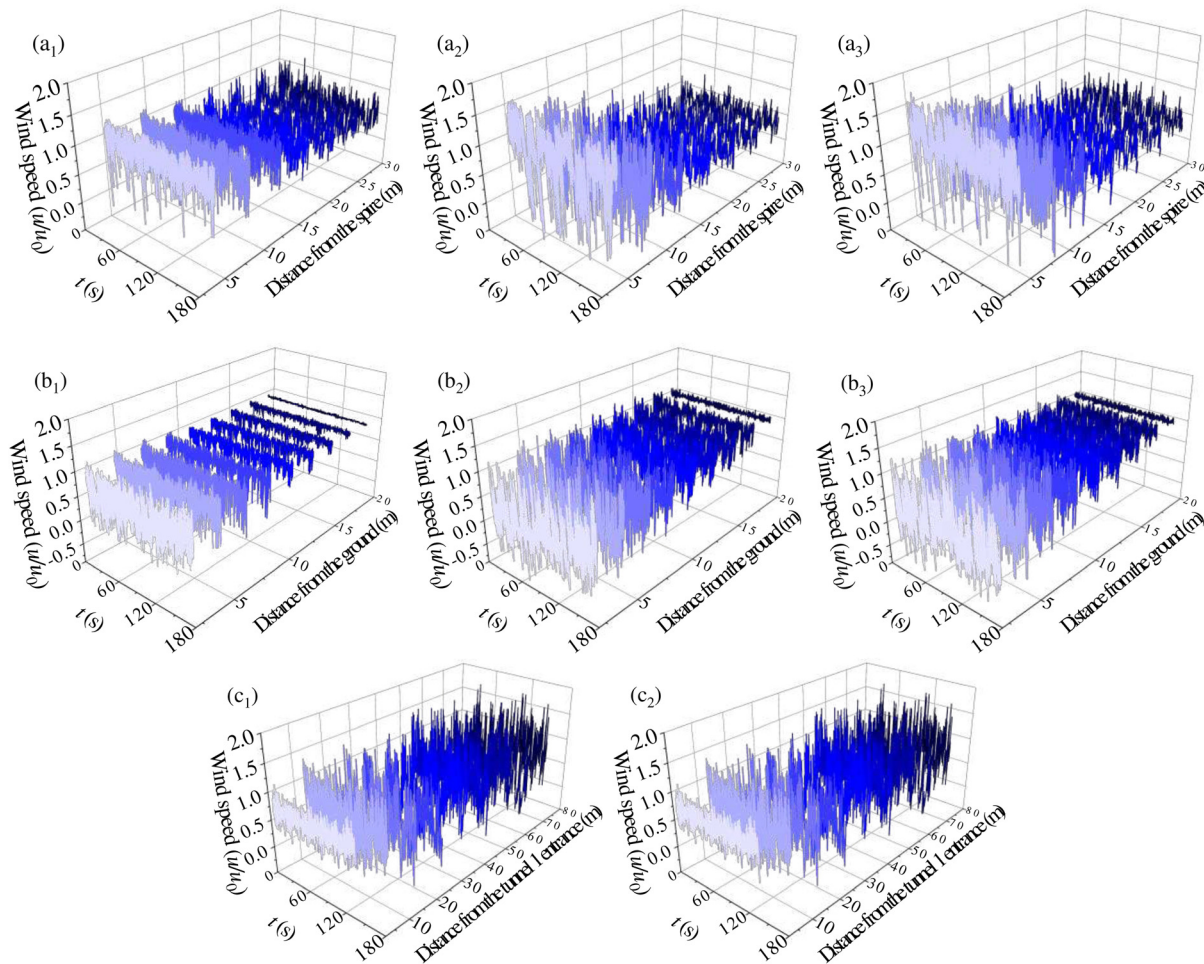


FIG. 12. Coefficient time history of turbulent wind speed generated by the spire: (a) direction of the incoming flow, (b) height direction, and (c) direction along the line.

P3 lines eventually decayed to 0.5. The average wind speed of P1 decreases to 0.65 due to the acceleration effect of the mountain wall. In the height direction, the wind speed gradually increases with the increase in height, P1 increases from 0.75 to 1, and P2 and P3 increases from 0.4 to 1.15. In the direction along the line, the wind speed of WSL at the tunnel entrance is 0.85, the wind speed of the corresponding leeward side line (LSL) is 0.35, and the average wind speed of the remaining measuring points is 0.5.

For the fence, in the direction of the incoming flow, the average wind speed of P2 and P3 near the fence can reach 1.55, and the average wind speed of P1 is 1.3. With the attenuation of turbulence, the average wind speed of P2 and P3 8.28 W away from the fence is 0.8; the average wind speeds on P1 at 4.14 and 6.89 W from the fence are reduced to 0.25 and 0.05, respectively, due to the lifting of the airflow tunnel door. In the height direction, at 0.65 H, the average wind speed of P1, P2, and P3 is 0.25. As height increases, the average wind speed of P1, P2, and P3 fluctuate in the range of 0.25–1.25, due to the geometry of the fence. In the direction along the line, the average wind speed on WSL is approximately 1.1. On LSL, the average wind speed at the

other locations is 0.85 except for the average wind speed at the tunnel entrance of 0.3.

Under the same blockage rate, the average wind speed on the leeward side of the spire decays more remarkably in the incoming flow direction compared with the results of the fence (except for P1, the other lines decay to a steady state at $2.76L$). However, the average wind speed on the P1 line of the fence model shows a substantial attenuation at $2.76L$. In the height direction, the wind speed simulated by the spire is closer to the wind speed profile,¹⁴ and the wind speed field simulated by the spire is more uniform. In the direction along the line, the average wind speeds of the windward and leeward lines of the fence are 60% and 43.75% higher than the corresponding value of the spire, respectively.

B. Turbulence characteristics

Figure 15 shows the turbulence intensity distribution of the incoming flow direction and the vertical direction of the three lines, as well as the windward and leeward lines in the line direction to

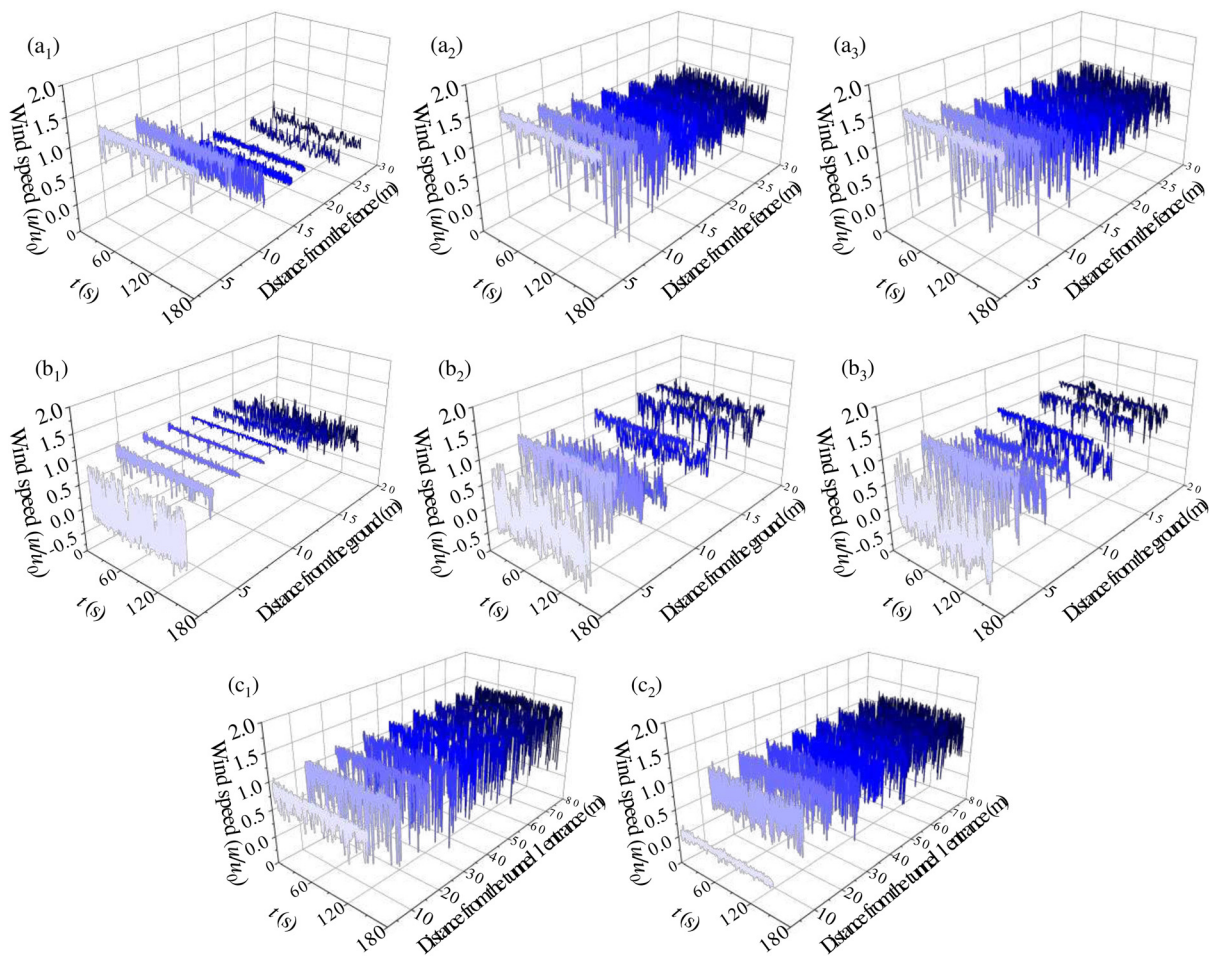


FIG. 13. Coefficient time history of turbulent wind speed generated by the fence: (a) direction of the incoming flow, (b) height direction, and (c) direction along the line.

determine the turbulence attenuation law of the incoming flow at the spire and fence.

For the spire, turbulence initially increases and then decays in the incoming flow direction.²¹ Among them, P2 and P3 reach the maximum at 2.76 W from the spire, and the corresponding peak value can reach eight times of the initial position. The possible reason is that the spacing between the bottom of the two spires is too small, and the tail vortices between the adjacent spires interfere strongly with each other. While the rise amplitude of P1 line is only about three times of the initial position. After reaching the peak value (1.4 W from the spire), the turbulence intensity attenuation law in the incoming flow direction is no longer obvious. The possible reason for this phenomenon is that the gap between the mountain wall and the spire nearest the tunnel entrance not only weakens the turbulence intensity but also weakens the dissipation of turbulent kinetic energy in the direction of the incoming flow. In the height direction, as height increases, turbulence intensity decreases (consistent with the law of ABL flow³). The reason is that the spire spacing increases with height, the interaction of tail vortices between adjacent spires decreases with the increase in height.

In the line direction, the turbulence intensity of the windward line changes alternately due to the difference in the wind field flow pattern between the leeward side of the spire and the middle area between the two spires. The highest value can reach 1.2, the lowest value can reach 0.2, the difference between the two is six times. The difference decreases with the increase in distance; thus, the turbulence intensity of the leeward line is evenly maintained at approximately 0.3. It is worth noting that this value is consistent with the representative value of turbulence intensity based on field test introduced in Sec. II C.

For the fence, the turbulence intensity in the incoming flow direction also shows a trend of increasing initially and then decreasing, reaching a maximum at 2.76 W from the fence and then decreasing slightly and maintaining a stable value. Compared with the spire, turbulence intensity changes more smoothly, and the peak value is less than half the corresponding value of the spire case. It is worth noting that due to the large spacing between the vertical ribs of the fence and the uniform distribution in the line direction, there is no significant difference in the turbulence law between P1, P2, and P3 in the direction of incoming flow. In the height direction, the turbulence intensity

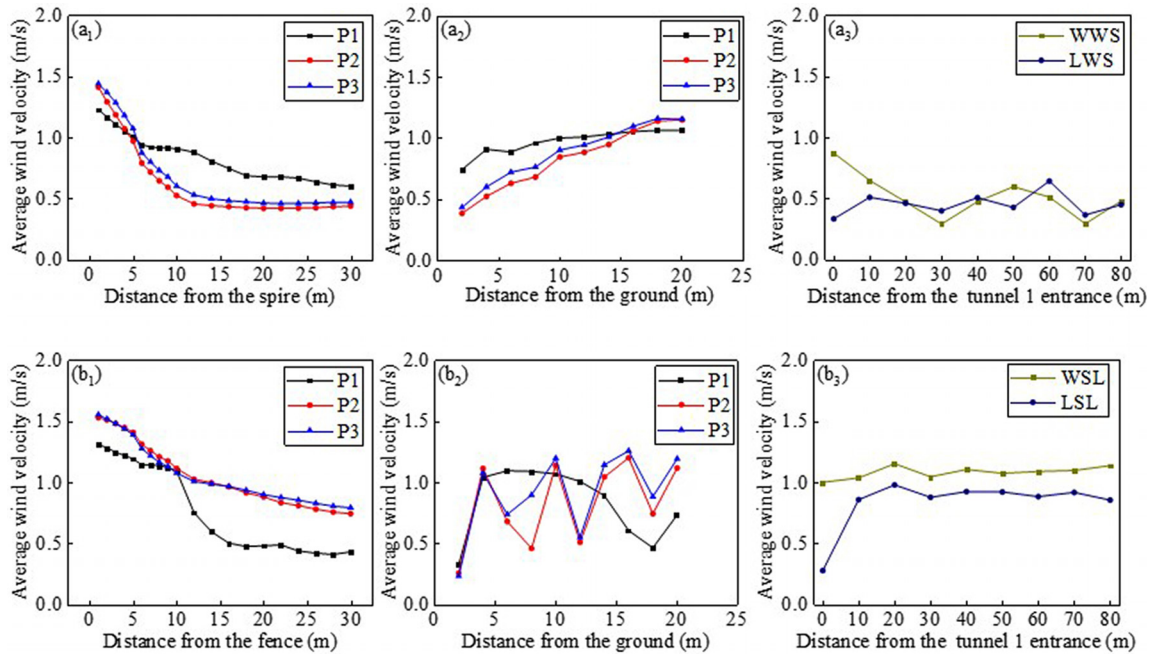


FIG. 14. Spatial distribution of 3D mean wind speed: (a) spire and (b) fence.

of the near-surface measuring point is the largest, and the turbulence intensity of the P3 measuring point is as high as 1.6. As height increases, turbulence intensity fluctuates in the range of 0–0.4 due to the equal distance between the transverse ribs of the fence. In the

direction of the line, the turbulence intensity of the line on the windward and leeward sides is stable at approximately 0.3 due to the rapid attenuation of the turbulence intensity on the leeward side of the fence.

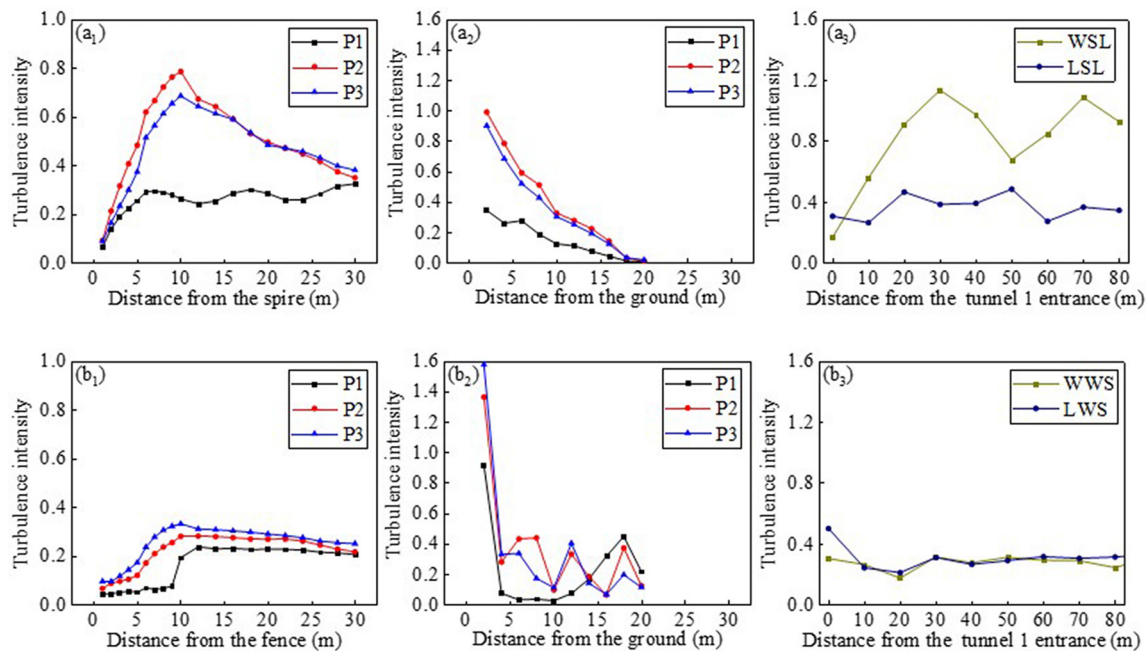


FIG. 15. Turbulence intensity for three survey lines: (a) spire and (b) fence.

In summary, from the perspective of turbulence intensity characteristics, both the spire and the fence can achieve the turbulence intensity level measured in the field, but the spire can obtain ABL characteristics consistent with similar studies, while the fence cannot.

C. Flow field

Figures 16 and 17 show the flow field of the spire and fence from the ground height of $y = 2.5$ m and the tunnel portal of $x = 0$ L (P1), 0.26 L (P2), and 0.52 L (P3) to reveal the transient flow field differences of the tunnel entrance section simulated by the spire and fence, respectively. Subscripts 1, 2, and 3 represent time of 100, 110, and 120 s, respectively. The corresponding transient turbulent kinetic energy (TKE) distribution of the two turbulence generators is shown in Figs. 18 and 19. TKE is defined as follows:

$$k = \frac{1}{2}(\tilde{u}^2 + \tilde{v}^2 + \tilde{w}^2), \quad (9)$$

where \tilde{u} , \tilde{v} , and \tilde{w} represents the root mean square of the three fluctuating wind speed components.

Figure 16 shows that for the section $y = 2.5$ m, the airflow at the tunnel entrance produces an acceleration effect, and the airflow accelerates through both sides of the spire to form turbulence in the middle of the line (dotted yellow frame in the picture). Moreover, the airflow blocked by the spire forms a vortex on the leeward side of the spire, and the wind speed is negative. For the P1 plane, low-speed flow is mainly distributed in the near-ground area. The airflow passes through

the spire to form a vortex, and then the vortex falls off and decays as it moves away from the spire. In the P2 and P3 planes, a larger range of acceleration zone is formed when the airflow passes through the spire, resulting in an average wind speed greater than the corresponding value of the P1 plane. With the attenuation of turbulence, at 2.76 W behind the spire, the average wind speed at the tunnel entrance is greater than that at the middle measuring point of the line, consistent with the measured value. On the leeward side of the spire, wind speed increases with the increase in height, and reaches the highest value at the top of the spire. Figure 18 shows a turbulent stratification zone is formed on the leeward side of the spire, and a strong TKE zone exists in a small range. Turbulence activity is very intense at the junction of the strong TKE region and the weak TKE region.

Figure 17(b) show that for the P1 plane, the airflow passes through the fence and the mountain wall to form a large-scale low-speed zone at the tunnel entrance, and the wind speed decreases rapidly along the flow direction, especially on the leeward side of the tunnel entrance, different from the measured value. For the P2 and P3 planes, compared with the spire, wind speed increases rapidly after airflow passes through the fence, and the wind speed of WSL is greater than the corresponding value of the spire. It worth noting that due to the existence of the transverse ribs of the fence, there is a small vortex area with negative wind speed in the corresponding area of the leeward side of the transverse ribs. This is the fundamental reason for the significant difference between the fence and the spire in the distribution of wind speed and turbulence intensity in the vertical direction. The following findings are obtained from Figs. 19(b) and 19(c): A larger range

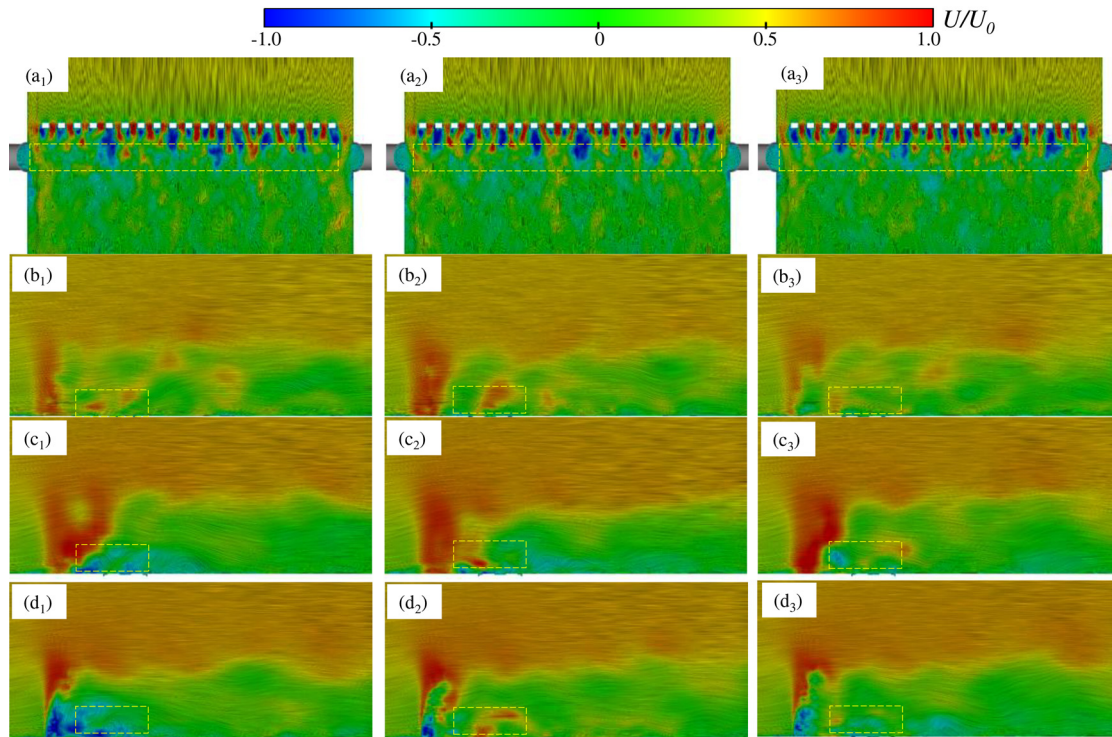


FIG. 16. Transient flow field of the spire: (a) section $y = 2.5$ m, (b) P1, (c) P2, and (d) P3.

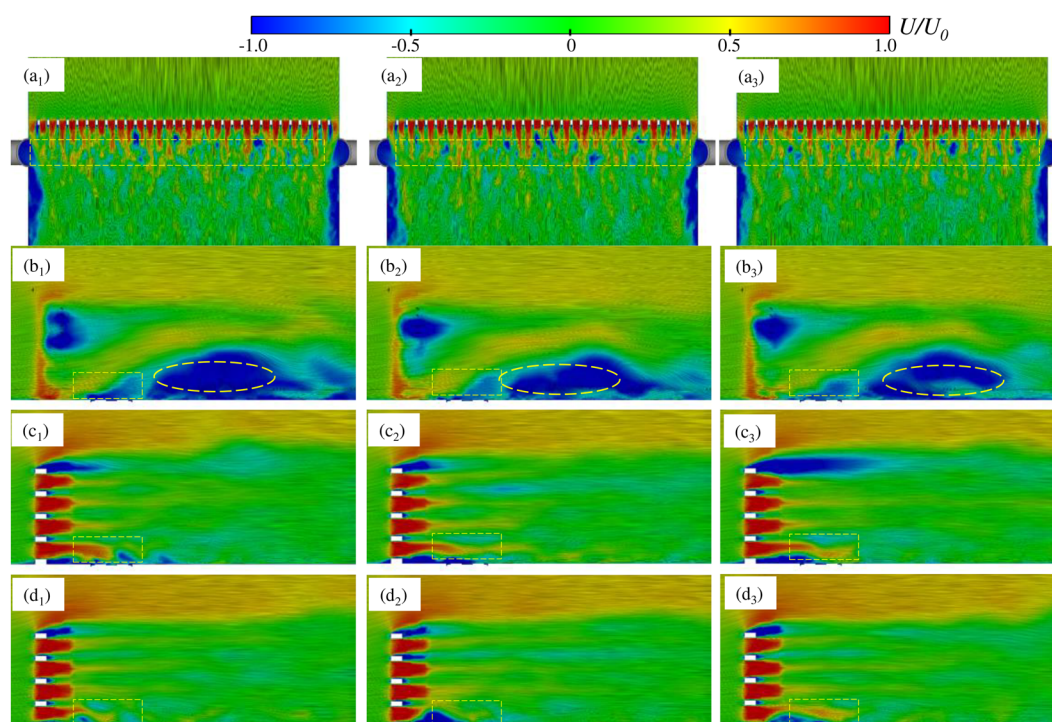


FIG. 17. Transient flow field of the fence: (a) section $y = 2.5$ m, (b) P1, (c) P2, and (d) P3.

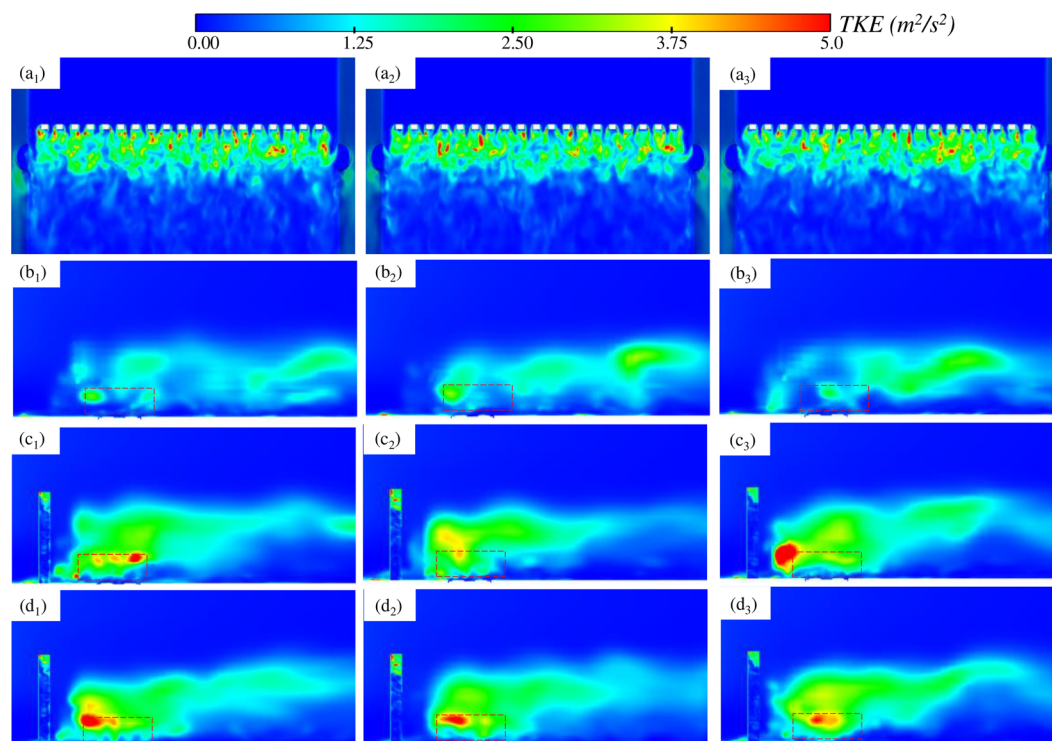


FIG. 18. TKE on leeward side of the spire: (a) section $y = 2.5$ m, (b) P1, (c) P2, and (d) P3.

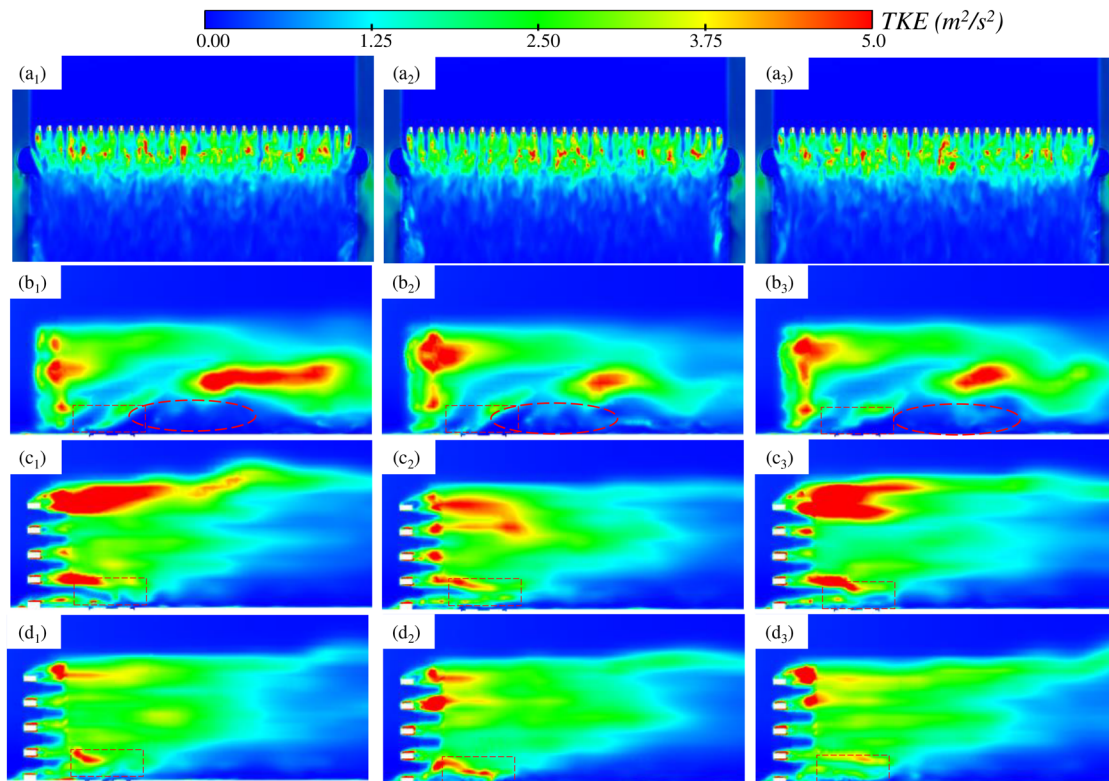


FIG. 19. TKE on leeward side of the fence: (a) section $y = 2.5$ m, (b) P1, (c) P2, and (d) P3.

of strong TKE area is formed on the leeward side of the fence, so the attenuation rate of wind speed on the leeward side of the fence is smaller than that on the leeward side of the spire, and the wind speed at the measuring point on the leeward side of the fence is greater than the corresponding value of the spire. With TKE attenuation, the turbulent intensity at the spire and fence on the leeward side is consistent.

D. Power spectral density

Figure 20 shows the power spectral density (PSD) curves of the measured 1# measuring point and the corresponding numerical

simulation P2 measuring point on WSL. The PSD curves of the measured and the spire numerical simulation are in better agreement, especially in the low frequency band. The wind power spectrum of the WSL of the fence numerical simulation P2 line is poorly consistent. The turbulence integral scale of the P2 measuring point simulated by the spire is 49.3 m, which is close to the measured results.

V. CONCLUSIONS

Based on the wind field test and IDDES methods, the present study used two kinds of geometric turbulence generators, namely,

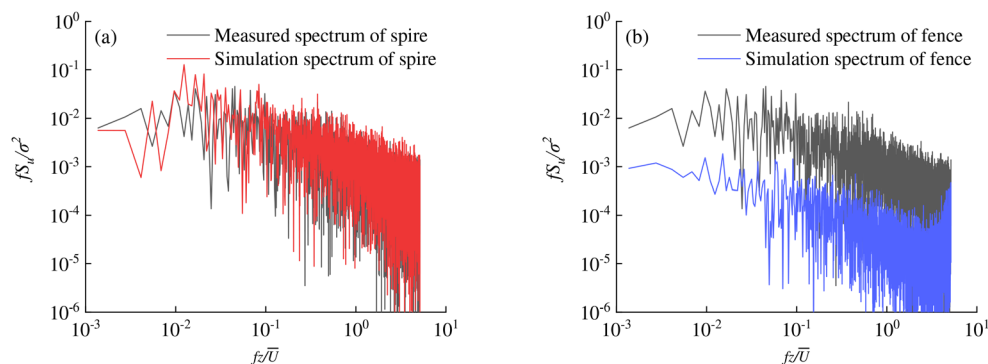


FIG. 20. Comparison of measured and simulated PSD curves: (a) spire and (b) fence.

spire and fence, to simulate the wind field of cross incoming flow at the tunnel entrance of TFT site. The difference law of turbulent wind field under two turbulence generator conditions was compared and analyzed. The main conclusions are as follows.

- (1) Based on the field test, the high wind speed section of the tunnel entrance is mainly 9–14 m/s, the prevailing wind direction is almost perpendicular to the line direction, and the representative value of turbulence intensity is 0.3.
- (2) Under the same blocking rate, the average wind speed on the leeward side of the spire decays more rapidly in the incoming flow direction. In the height direction, the wind speed simulated by the spire is more suitable for the wind speed profile. In the direction along the line, the average wind speed of the windward and leeward lines of the fence are 60% and 43.75% higher than the corresponding values of the spire, respectively.
- (3) In the direction of incoming flow, the turbulence intensity of the turbulent wind generated by the spire and the fence increases initially and then decreases, reaching the maximum at 2.76 W from the spire and the fence. The turbulence intensity of the windward side of the spire is large and fluctuates along the line, and the turbulence intensity of the leeward line is evenly maintained at 0.3. The turbulence intensity of the turbulence wind generated by the fence is more stable, and the turbulence intensity of the windward and leeward lines is stable at 0.3.
- (4) For the PSD, the turbulent wind simulated by the numerical simulation of the spire is in better agreement with the measured results at the corresponding position, especially in the low frequency band.

ACKNOWLEDGMENTS

This work was funded by the National Natural Science Foundation of China (Grant Nos. 51978670 and U1934209), the National Outstanding Youth Science Fund Project of National Natural Science Foundation of China (Grant No. 51925808), the Research Grants Council, University Grants Committee of the Hong Kong Special Administrative Region (SAR), China (Grant No. R-5020-18), the Innovation and Technology Commission of the Hong Kong SAR Government (Grant No. K-BBY1), and The Hong Kong Polytechnic University's Postdoc Matching Fund Scheme (Grant No. 1-W21Q). The numerical calculations in this paper have been done on the Hefei advanced computing center.

AUTHOR DECLARATIONS

Conflict of Interest

The authors have no conflicts to disclose.

Author Contributions

E Deng: Conceptualization (lead); Data curation (lead); Funding acquisition (equal); Writing – original draft (equal). **Huan Yue:** Formal analysis (equal); Investigation (equal); Software (equal); Writing – original draft (lead). **Yi-Qing Ni:** Funding acquisition (lead); Writing – review & editing (lead). **You-Wu Wang:** Resources (lead); Supervision (lead); Writing – review & editing (equal). **Xuhui**

He: Funding acquisition (equal); Writing – review & editing (equal). **Zheng-Wei Chen:** Writing – review & editing (equal).

DATA AVAILABILITY

The data that support the findings of this study are available from the corresponding author upon reasonable request.

REFERENCES

- ¹W. C. Yang, H. Yue, E. Deng, X. H. He, Y. F. Zou, and Y. W. Wang, "Comparison of aerodynamic performance of high-speed train driving on tunnel-bridge section under fluctuating winds based on three turbulence models," *J. Wind Eng. Ind. Aerodyn.* **228**, 105081 (2022).
- ²T. Li, M. G. Yu, J. Y. Zhang, and W. H. Zhang, "A fast equilibrium state approach to determine interaction between stochastic crosswinds and high-speed trains," *J. Wind Eng. Ind. Aerodyn.* **143**, 91–104 (2015).
- ³H. Kozmar and B. Laschka, "Wind-tunnel modeling of wind loads on structures using truncated vortex generators," *J. Fluids Struct.* **87**, 334–353 (2019).
- ⁴X. Xue, H. D. Yao, and L. Davidson, "Synthetic turbulence generator for lattice Boltzmann method at the interface between RANS and LES," *Phys. Fluids* **34**, 055118 (2022).
- ⁵L. Shen, Y. Han, C. S. Cai, G. C. Dong, J. R. Zhang, and P. Hu, "LES of wind environments in urban residential areas based on an inflow turbulence generating approach," *Wind Struct.* **24**(1), 1–24 (2017).
- ⁶S. B. Du, M. S. Li, and Y. Yang, "Effects of turbulence integral scales on characteristics of fluctuating wind pressures," *J. Wind Eng. Ind. Aerodyn.* **204**, 104245 (2020).
- ⁷Y. G. Li, J. H. Yan, Y. Li, C. X. Xiao, and J. X. Ma, "Wind tunnel study of wind effects on 90° helical and square tall buildings: A comparative study," *J. Build. Eng.* **42**, 103068 (2021).
- ⁸Y. Tominaga and M. Shirzadi, "Wind tunnel measurement of three-dimensional turbulent flow structures around a building group: Impact of high-rise buildings on pedestrian wind environment," *Build. Environ.* **206**, 108389 (2021).
- ⁹P. Górski, M. Tatara, S. Pospíšil, and A. Trush, "Aerodynamic force coefficients of an ice-accreted bridge cable in low and moderately turbulent wind," *J. Wind Eng. Ind. Aerodyn.* **205**, 104335 (2020).
- ¹⁰A. H. Dawi and R. A. D. Akkermans, "Direct noise computation of a generic vehicle model using a finite volume method," *Comput. Fluids* **191**, 104243 (2019).
- ¹¹A. F. Melaku and G. T. Bitsuamlak, "A divergence-free inflow turbulence generator using spectral representation method for large-eddy simulation of ABL flows," *J. Wind Eng. Ind. Aerodyn.* **212**, 104580 (2021).
- ¹²W. C. Hu, Q. S. Yang, H. P. Chen, Z. T. Yuan, C. Li, S. Shao, and J. Zhang, "Wind field characteristics over hilly and complex terrain in turbulent boundary layers," *Energy* **224**, 120070 (2021).
- ¹³F. Cheli, S. Giappino, L. Rosa, G. Tomasini, and M. Villani, "Experimental study on the aerodynamic forces on railway vehicles in presence of turbulence," *J. Wind Eng. Ind. Aerodyn.* **123**, 311–316 (2013).
- ¹⁴J. Q. Niu, D. Zhou, and X. F. Liang, "Experimental research on the aerodynamic characteristics of a high-speed train under different turbulence conditions," *Exp. Therm. Fluid Sci.* **80**, 117–125 (2017).
- ¹⁵Y. H. Noguchi, M. Suzuki, C. Baker, and K. Nakade, "Numerical and experimental study on the aerodynamic force coefficients of railway vehicles on an embankment in crosswind," *J. Wind Eng. Ind. Aerodyn.* **184**, 90–105 (2019).
- ¹⁶S. Y. Zhu, Y. L. Li, and X. Y. Xu, "Wind tunnel test on the aerodynamic admittance of a rail vehicle in crosswinds," *J. Wind Eng. Ind. Aerodyn.* **226**, 105052 (2022).
- ¹⁷W. C. Yang, Y. K. Liu, E. Deng, Y. W. Wang, X. H. He, M. F. Lei, and Y. F. Zou, "Field test and numerical reconstitution of natural winds at the tunnel entrance section of high-speed railway," *Int. J. Numer. Methods Heat Fluid Flow* **23**(2), 617–647 (2022).
- ¹⁸W. C. Yang, Y. K. Liu, E. Deng, Y. W. Wang, X. H. He, and M. F. Lei, "Characteristics of wind field at tunnel-bridge area in steep valley: Field measurement and LES study," *Measurement* **202**, 111806 (2022).

¹⁹W. C. Yang, H. Yue, E. Deng, Y. W. Wang, X. H. He, and Y. F. Zou, "Influence of the turbulence conditions of crosswind on the aerodynamic responses of the train when running at tunnel-bridge-tunnel," *J. Wind Eng. Ind. Aerodyn.* **229**, 105138 (2022).

²⁰T. Y. Dong, M. Guglielmo, J. B. Wang, X. F. Liang, and S. Krajnović, "Numerical investigation of a high-speed train underbody flows: Studying flow

structures through large-eddy simulation and assessment of steady and unsteady Reynolds-averaged Navier–Stokes and improved delayed detached eddy simulation performance," *Phys. Fluids* **34**, 015126 (2022).

²¹G. Chen, X. B. Li, and X. F. Liang, "IDDES simulation of the performance and wake dynamics of the wind turbines under different turbulent inflow conditions," *Energy* **238**, 121772 (2022).